Title	Characteristics of CME- and CIR-driven ion upflows in the polar ionosphere
Authors	Ogawa Yasunobu, Seki Kanako, Keika Kunihiro, Ebihara Yusuke
Citation	JGR : Space Physics, 124(5), 3637-3649, 2019
Issue Date	2019-4-15
Type	Journal Article
URL	https://doi.org/10.1029/2018JA025870
Right	
Textversion	publisher

JGR Space Physics

RESEARCH ARTICLE
10.1029/2018JA025870

Characteristics of CME- and CIR-Driven Ion Upflows in the Polar Ionosphere

Y. Ogawa[1,2], K. Seki[3], K. Keika[3], and Y. Ebihara[4]

[1]National Institute of Polar Research, Tokyo, Japan, [2]Graduate University for Advanced Studies (SOKENDAI), Kanagawa, Japan, [3]Graduate School of Science, Department of Earth and Planetary Science, University of Tokyo, Tokyo, Japan, [4]Research Institute for Sustainable Humanosphere, Kyoto University, Kyoto, Japan

Key Points:
- Flux and velocity of ionospheric ion upflows during magnetic storms are quantitatively examined
- CME-driven storms have about 4 times larger upward ion flux in the nighttime than those under CIR-driven storms
- Dayside ion upflows under small CIR-driven storms continue a few days longer than those under small CME-driven storms

Supporting Information:
- Supporting Information S1

Correspondence to:
Y. Ogawa,
yogawa@nipr.ac.jp

Citation:
Ogawa, Y., Seki, K., Keika, K., & Ebihara, Y. (2019). Characteristics of CME- and CIR-driven ion upflows in the polar ionosphere. *Journal of Geophysical Research: Space Physics*, *124*, 3637–3649. https://doi.org/10.1029/2018JA025870

Received 5 JUL 2018
Accepted 7 APR 2019
Accepted article online 15 April 2019
Published online 13 MAY 2019
Corrected 27 AUG 2019

This article was corrected on 27 AUG 2019. See the end of the full text for details.

Abstract We investigated how velocity and flux of ionospheric ion upflows vary during magnetic storms driven by corotating interaction regions (CIRs) and coronal mass ejections (CMEs), using data from the European Incoherent Scatter (EISCAT) Tromsø UHF and Svalbard radars between 1996 and 2015. The characteristics of ion upflows were compared with ion and electron temperature variations measured with the EISCAT radars and also joule heating rate, electric field, and field-aligned current distribution derived from the Weimer model. Upward ion velocity increases in the nighttime at Tromsø (66.2 °N geomagnetic latitude) just after the CIR- and CME-driven storms, corresponding to electron temperature enhancements due to soft particle precipitation and also ion temperature enhancements in the strong westward electric field region. The CME-driven storms have larger upward ion flux (~1.7×10^{13} $m^{-2}s^{-1}$) than those under the CIR-driven storms (~0.3×10^{13} $m^{-2}s^{-1}$). In the daytime, ion upflows are seen at Longyearbyen, Svalbard (75.2 °N geomagnetic latitude), with an upward flux of typically 10^{13} $m^{-2}s^{-1}$ for small CIR and CME storm cases. Substantial ion upflows last for a few days after the storm onsets under small CIR storms, whereas they last for only a day under small CME storms. Under both the cases, the substantial ion upflows are associated with an enhancement of the Region 1 field-aligned current, eastward electric field and Joule heating rate. For large CME storms, substantial ion upflows are absent in the daytime probably due to equatorward expansion of the auroral oval.

1. Introduction

It is well known that ionospheric ions gain kinetic energy and electromagnetic energy originating from the solar wind and escape from the polar ionosphere to the magnetosphere. Its escape rate has been estimated using several methods such as in situ measurements and modeling (e.g., Ebihara et al., 2006; Engwall et al., 2009; Seki et al., 2001). When magnetic storms occur, velocity and flux of the escaping ions largely increase. Oxygen ions originated from the ionosphere are fed into the plasma sheet as well as the inner magnetosphere. The energy density of the oxygen ions can become dominant in the ring current (e.g., Gloeckler et al., 1985; Hamilton et al., 1988; Keika et al., 2013) and in the plasma sheet (Nosé et al., 2001, 2005) during magnetic storms.

In the polar ionosphere, ion upflow is frequently seen during auroral substorm (e.g., Ogawa et al., 2013), which is most likely associated with the ion outflow measured in the bottomside magnetosphere (Wilson et al., 2004). A typical duration of a substorm is about a few hours. Multiple substorms happen recurrently during the main phase of magnetic storms. Thus, continued and substantial ion upflows are expected during the storm main phase. Coley and Heelis (2009) showed characteristics of the vertical ion flux of thermal O^+ in the topside high-latitude ionosphere before and during magnetic storms using data from the DMSP spacecraft. They revealed a pattern of a sharp increase in upward fluxes at storm onset with a more gradual increase in downward fluxes. However, it is not fully understood mechanisms of ion upflows in the topside ionosphere during the magnetic storms. A previous case study shows strong ion upflows associated with soft (<500 eV) particle precipitation during the main phase and the beginning of the recovery phase of magnetic storms (Liu et al., 2000). However, effects of storms on ion upflows have not been systematically investigated because of a limited number of data sets. Thus, it had been difficult to understand long-timescale processes of ion escape from the topside ionosphere to the bottomside magnetosphere.

There are two types of solar wind driver for the magnetic storms. One is driven by coronal mass ejection (CME). The other is driven by corotating interaction region (CIR). The CIR-driven storms have hotter

plasmas and produce high fluxes of relativistic electrons, whereas the CME-driven storms have denser plasma sheets and strong ring currents (e.g., Borovsky & Denton, 2006). Cosmic noise absorption observations indicate that particle (>30-keV electron) precipitation is more intense during the main phase of CME-driven storms, but the precipitation remains elevated for a much longer period during CIR-driven storms (Longden et al., 2008). During the CIR-driven storms, cosmic noise absorption caused by energetic particle precipitation is increased at high latitudes between 21 and 15 magnetic local time (MLT) during several days after the high-speed solar wind streams impact (Grandin et al., 2017; Kavanagh et al., 2012). Such high-energy precipitation causes ionization in the *D* and *E* region ionosphere. Thus, there are some differences between the CME-driven magnetic storms and the CIR-driven magnetic storms regarding impacts on the magnetosphere and the ionosphere (e.g., Borovsky & Denton, 2006; Miyoshi et al., 2013). It is therefore important to understand quantitatively the impacts of the CME-driven storms and the CIR-driven storms on the ion upflows.

Here we report an investigation of storm effects on the ionospheric ion upflow, using a 20-year data set of the European Incoherent Scatter (EISCAT) radars at two locations in Tromsø, Norway, and Longyearbyen, Svalbard. The EISCAT radars are one of the most powerful tools for the ion upflow investigation because they enable us to derive the field-aligned ion velocity and flux in the polar topside ionosphere.

The organization of this paper is as follows. In section 2, we describe the EISCAT and other data sets used in this study. In section 3, observational results of ion upflows at two locations are shown. It was found that some characteristics of ion upflow during CIR-driven storms are different from those during CME-driven storms. In section 4, we discuss what causes the difference based on the relation between the observational positions, convection pattern, and large-scale field-aligned currents. The conclusions are provided in section 5.

2. Data Set

This study used the ionospheric plasma data obtained with the EISCAT Tromsø UHF radar (located at the geomagnetic latitude of 66.2 °N, the geographic latitude of 69.6 °N, and the geographic longitude of 19.2 °E) and the EISCAT Svalbard radar (located at the geomagnetic latitude of 75.2 °N, the geographic latitude of 78.2 °N, and the geographic longitude of 16.0 °E) between 1996 and 2015. We chose the EISCAT data obtained at altitudes between 400 and 500 km only when the radars are looking along the local magnetic field line, and then we integrated their autocorrelation function (ACF) data for 5 min to derive plasma parameters for this study. The altitude resolution of the analyzed data between 400- and 500-km altitude was approximately 50 km, and an average value at about 420- and 470-km altitudes was used in this study. The electron density data obtained at Tromsø were calibrated with dynasonde (Rietveld et al., 2008), and those at Logyearbyen were calibrated with plasma line data when they are available. Their calibration errors were roughly 20%. We also screened data when fitting results were unrealistic values: Absolute value of ion velocity was more than 1,500 m/s, electron density was more than 10^{13} m^{-3}, or electron density was less than 10^{10} m^{-3}.

In order to understand the relative location of the radar under various geomagnetic conditions, the Weimer empirical model (Weimer, 2005) was used in this study. The model provides field-aligned current (FAC), ionospheric electric field, and Joule heating rate. The input parameters are the interplanetary magnetic field (IMF), the solar wind velocity, the solar wind dynamic pressure, and the AL index. We used the OMNI data base for the solar wind data. Time resolution of the solar wind parameters was 5 min. In the Weimer model, the electric and magnetic potentials are expressed by a Fourier series. From the magnetic potential, one can calculate the FAC density and the magnetic disturbance. From the magnetic disturbance and the electric field, one can calculate the incident Poynting flux above the ionosphere. The incident Poynting flux is assumed to be equal to the Joule heating rate in the ionosphere. We derived the FAC, the ionospheric electric field, and the Joule heating rate for the EISCAT radar locations at the moment when the EISCAT observation data is available, in order to relate characteristics of ion upflows observed with the EISCAT radars and the possible conditions in the ionosphere and the magnetosphere.

For this study, we used the storm list published by Kataoka and Miyoshi (2006) who classified the magnetic storms occurred during the interval between 1996 and 2005 into CME-driven storms, CIR-driven storms, or other storms. Their list includes the magnetic storms with the Dst minimum being less than −100 nT. As for

the storms occurred during the interval between 2006 and 2015, we added the storm list with the same criteria as those used by Kataoka and Miyoshi (2006). We also investigated the CME-driven and CIR-driven storms that occurred between 2006 and 2015 with the Dst minimum between −30 and −100 nT, to investigate the response of ion upflows on small storms. Each number of EISCAT data during CME-driven CIR-driven storm is described in the next section and the supporting information.

3. Results

3.1. Characteristics of Ion Upflows at 66.2 °N Geomagnetic Latitude

The geomagnetic latitude of 66.2 °N measuring with the EISCAT Tromsø UHF radar is a typical region located within nightside auroral oval and subauroral region in the dayside. Therefore, ion upflows have been frequently seen in the nightside at this latitude (e.g., Endo et al., 2000; Foster et al., 1998; Keating et al., 1990; Ogawa et al., 2010). We will explain characteristics of ion upflows and ion/electron temperature changes at 66.2 °N geomagnetic latitude under CIR- and CME-driven storms and difference of ion upflows under different sizes of magnetic storms.

Figure 1 shows averaged field-aligned ion velocity, ion flux, and ion and electron temperatures during the CIR-driven storms. They were measured by the EISCAT Tromsø UHF radar at altitudes between 400 and 500 km from 1996 to 2015. The EISCAT data between $T-3$ days and $T+5$ days are accumulated and averaged over a day, where T is onset time of a storm. The onset time T is defined as the arrival time of the shocks (stream interface) for CME- (CIR-) driven storms. The horizontal axis of the figure indicates time from the onset time T. The bin ranging between "zero" and "one" in the horizontal axis indicates the first 24 hr from the onset time T. Contribution from the data obtained under small storms (Dst minimum > ~−100 nT) to each bin is large because the number of the large CIR-driven storms (Dst minimum < ~−100 nT) is very small (which results in the number of EISCAT data under Dst minimum < ~−100 nT being less than three storms). We excluded data when the previous storm remains between $T-3$ days and $T+5$ days. The numbers of samples were about 500–1,500 on average (see panel a2 of Figure S1 in the supporting information). The number of samples in the morning becomes small (less than five events) on the third and fourth days of storm onset. When the number of sample dates was less than three, we discarded those samples and left the bin blank (panels a1, b1, c1, and d1). Upward ion velocity becomes large in the dusk and nightside regions just after the storm onset (panels a1 and a2). Their upward ion fluxes are relatively small (~0.3×10^{13} $m^{-2}s^{-1}$), due to low ion density at altitudes between 400 and 500 km. Ion velocities in the dawn region (03–09 MLT) are continuously upward (~50 m/s) before and after the storm onset, but their upward fluxes are very small (<0.2×10^{13} $m^{-2}s^{-1}$) because of very low ion density in the dawn region. An increase in ion temperature, from 1000 to 1500 K (i.e., by 500 K), is seen in the dawn region at the storm onset (panels c1 and c2), whereas some increases in ion temperatures are seen in the nighttime. Electron temperature is typically increasing in the dawn and nighttime region on the first day of the storm onset (from about 1500 to 1800–2200 K) and also enhanced in the dusk and daytime regions on the second day of the storm onset (panels d1 and d2).

Figure 2 is the same as Figure 1 except for the CME-driven storms. Contribution from the data obtained during large storms (−500 < Dst minimum < −100 nT) is large because the number of the small CME-driven storms (Dst minimum > ~−100 nT) is very little. Also, the numbers of samples are mostly less than 300 in the morning and daytime from the second to fourth days of the CME-driven storm onset (see panel b2 of Figure S1). Upward ion velocity becomes slightly increasing at all MLT sectors just after the storm onset, and upward flux dramatically increases in the nighttime (1.7×10^{13} $m^{-2}s^{-1}$), due to increased ion density in the topside ionosphere. The upward flux drastically decreases on the second and third days of storm. Ion and electron temperatures show similar characteristics of the ion velocity variations, indicating that the enhancements of frictional heating and heat flux/soft particle precipitation occur on the first day of storm onset. Ion temperature increases in the nighttime are from about 1300 to 1700 K (i.e., by 400 K) and then it is concluded that ion temperature enhancement in the nighttime is about 2 times larger than those under CIR-driven storm. Note that electron temperature is always high in the daytime due to solar illumination. Also, note that upward ion velocity and flux are seen in the nighttime region a few days before the CME-driven storm onset. Because we excluded multiple storm events from the data set, those upward velocity and flux between $T-3$ days and $T-1$ days are probably related to the isolated substorms that could occur during nonstorm times.

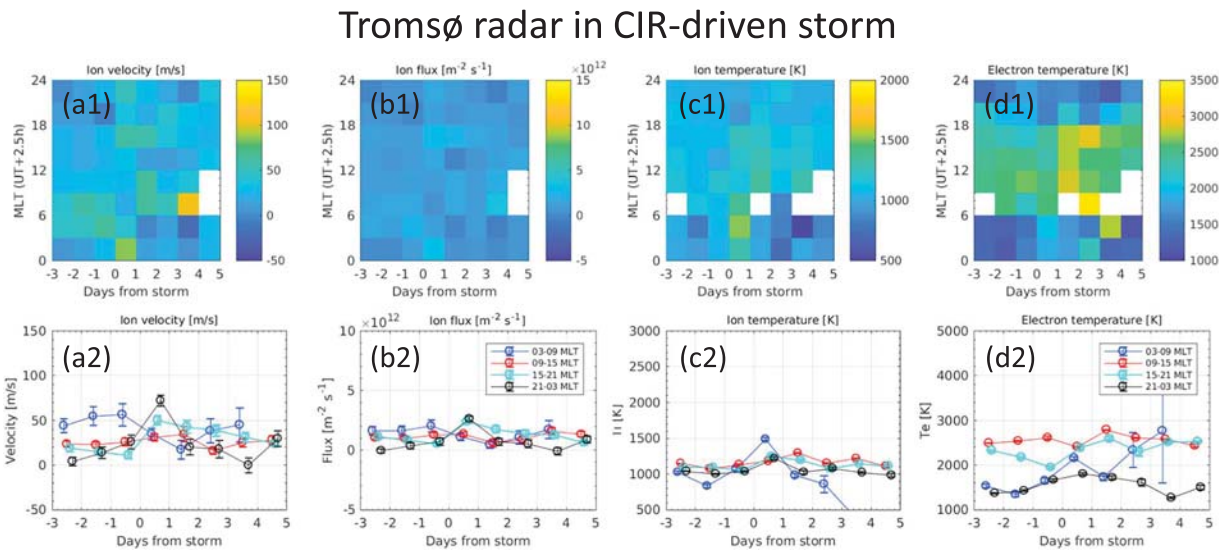

Figure 1. Averaged ion velocity, ion flux, ion temperature, and electron temperature during the CIR-driven storms measured with the EISCAT Tromsø UHF radar at 66.2 °N geomagnetic latitude between 1996 and 2015. Horizontal axis indicates days from the beginning of the storm. Vertical axis in upper panels (a1, b1, c1, and d1) is MLT. MLT at Tromsø is UT plus 2.5 hours. In lower panels (a2, b2, c2, and d2), averaged values at 03–09, 09–15, 15–21, and 21–03 MLT are plotted with blue, red, cyan, and black colors, respectively. Vertical bars indicate the standard errors of the mean. MLT = magnetic local time; UT = Universal time.

Figure 3 summarizes upflow velocity and flux sorted by small/large storms and CIR-driven/CME-driven storms. The number of samples for some of the categories is less than 250 (see Figure S2). However, the main region of ion upflows in Tromsø is nighttime, which often has the best statistics, so this is good for the comparison of ion upflow flux behavior between small and large storms. We discarded average values when the number of sample dates was less than three. As for the CIR-driven storms, major characteristics of ion velocity and flux seem to be independent of the scale of the storms (panels a1, b1, a2, and b2), except for those in the dusk side after the storm onset. Ion upflow occurs in the nighttime on the first day of the storm onset. As for the CME-driven storms, upward ion flux in the nighttime on the first day of storm depends clearly on the scale of storms (panels b3 and b4), although upward velocity is almost the same (~50 m/s) for both the small and the large magnetic storms (panels a3 and a4). Even under the CME-driven smaller storms (Dst minimum > −100 nT), the upward ion flux in the nighttime on the first day of storm is 0.7×10^{13} $m^{-2}s^{-1}$

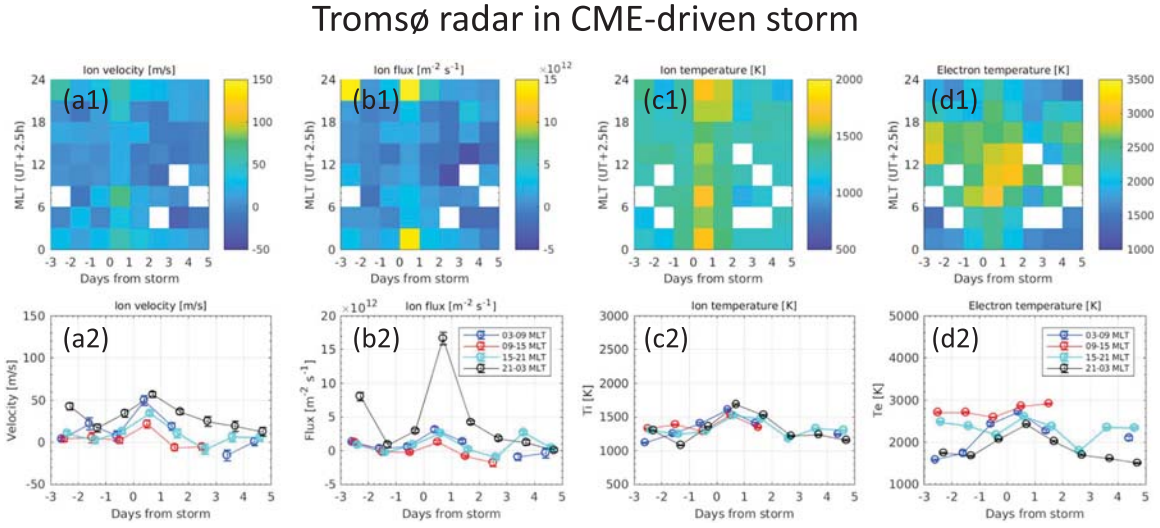

Figure 2. Same as Figure 1 except for CME-driven storms. MLT = magnetic local time; UT = Universal time.

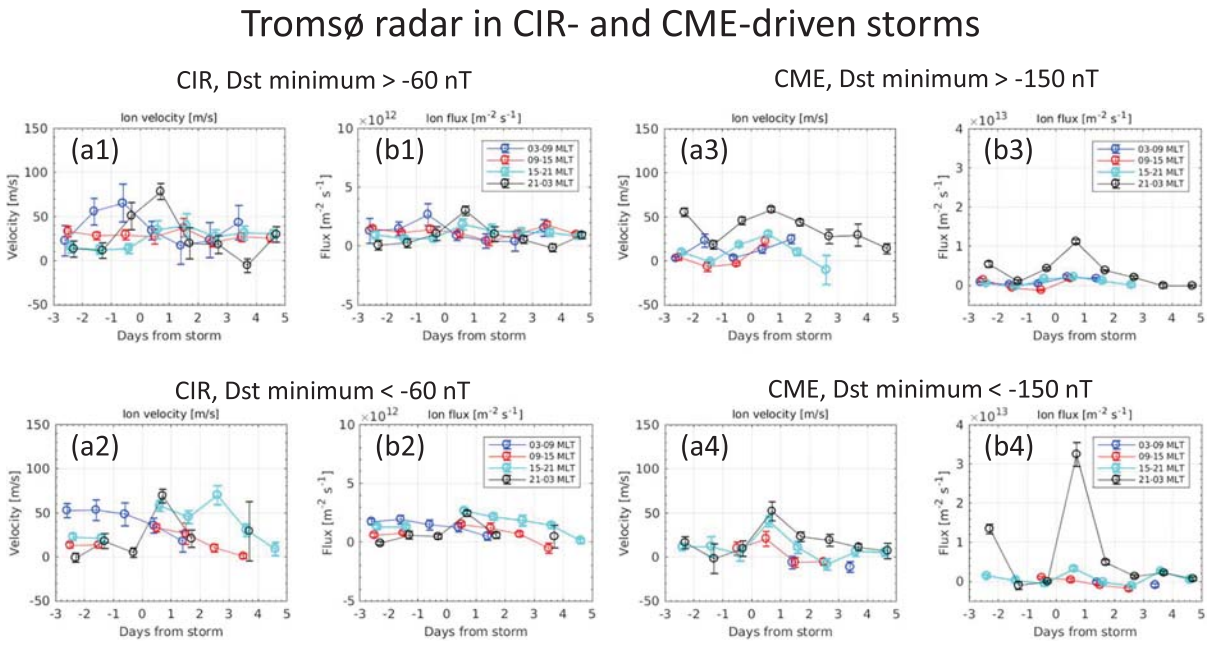

Figure 3. Averaged ion velocity and flux measured with the EISCAT Tromsø UHF radar. Formats of each panels is same as the panels a2 and b2 of Figures 1 and 2. They are divided into four categories: (a1 and b1) CIR-driven small storms (Dst minimum > −60 nT), (a2 and b2) CIR-driven large storms (Dst minimum < −60 nT), (a3 and b3) CME-driven small storms (Dst minimum > −150 nT), and (a4 and b4) CME-driven large storms (Dst minimum < −150 nT). CIR = corotating interaction region; CME = coronal mass ejection; MLT = magnetic local time.

(not shown here), which is clearly larger than that under the CIR-driven large storms (Dst minimum < −60 nT, panel b2).

3.2. Characteristics of Ion Upflows at 75.2 °N geomagnetic latitude

While the EISCAT Tromsø radar at 66.2 °N geomagnetic latitude mainly measures ion upflows in the nightside auroral oval, the EISCAT Svalbard radar observations at 75.2 °N geomagnetic latitude have an advantage to measure ion upflows in the vicinity of the dayside cusp and polar cap regions (e.g., Ogawa et al., 2009). In the dayside, radar location relative to several magnetospheric regions is important to interpret results obtained at a fixed latitude (e.g., Nilsson et al., 1996; Ogawa et al., 2003).

Figure 4 shows the field-aligned ion velocity, the ion flux, the ion temperature, and the electron temperature at the Svalbard radar during the CIR-driven storms. The numbers of samples for CIR-driven storms were always more than 1,500 (see panel c2 of Figure S1). Clear differences of upward ion velocity and flux between before and after the CIR storms are seen in the daytime (panels a2 and b2). Just after the CIR storms, averaged ion velocity and flux in the daytime increase up to 80 m/s and 0.9×10^{13} $m^{-2}s^{-1}$ at 400~500 km altitude, respectively. The averaged velocity decreases with time but keeps upward (~60 m/s) for a few days. The upward flux becomes ~0.4×10^{13} $m^{-2}s^{-1}$. Ion temperature becomes slightly elevated on the first day of storms, in particular, on the dawnside and dayside. The high temperature lasts for a few days. Electron temperature also increases at the storm onset and gradually decreases for a few days. The electron temperature differences are approximately 600 K in the daytime and 300–400 K in the other time periods.

Figure 5 is the same as Figure 4 except for the CME-driven storms. The characteristics of upflows during the CME-driven storms are clearly different from those during the CIR-driven storms. Small upward velocities (less than 50 m/s) are seen before the CME-driven storms and during the first day of the storm onsets, but they become close to zero one day after the onsets. Ion fluxes are largely upward in the nighttime at the storm onsets (~1.2×10^{13} $m^{-2}s^{-1}$), but they are almost zero or downward after the storm onsets. Ion temperature becomes elevated on the whole until 2 days after the CME-driven storm onsets. Electron temperature has no apparent difference between before and after the storm and decreases 3 days after the storm onsets. Note that the number of ESR data samples for the CME-driven storms was often more than 1,000

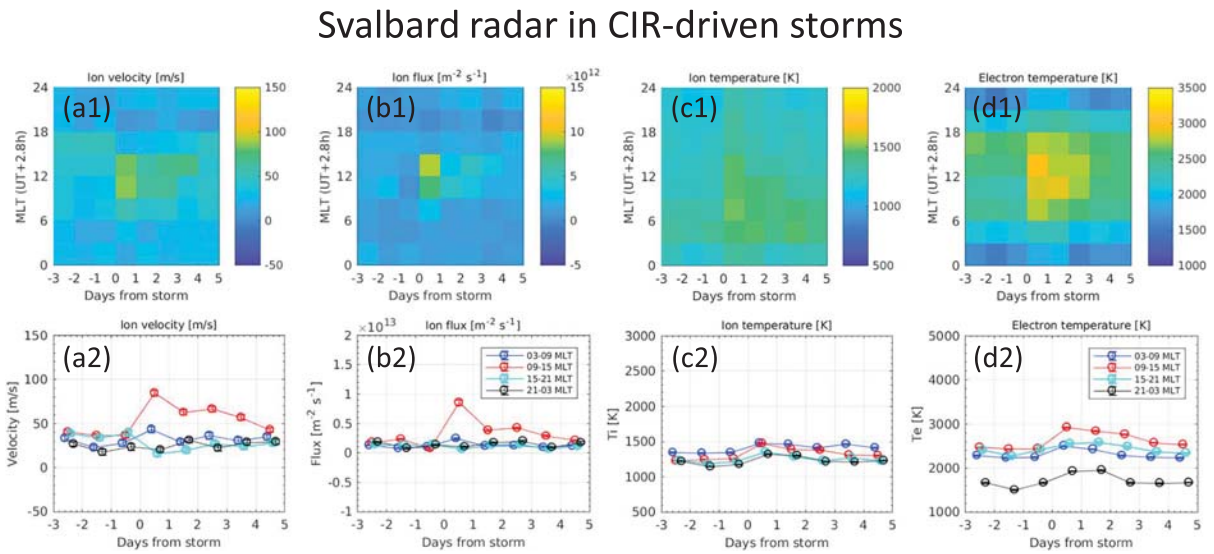

Figure 4. Same as Figure 1 except for the EISCAT Svalbard radar at 75.2 °N magnetic latitude between 1996 and 2015. MLT at the Svalbard radar location is UT plus 2.8 hr. Formats of the plots are same as those of Figure 1. CIR = corotating interaction region; MLT = magnetic local time; UT = Universal time.

for 1 day after the storm onset and earlier periods, but the numbers became small (less than 1,000) 2–4 days after the storm onset (see panel d2 of Figure S1). Thus, the change of number of samples/dates might cause the changes of electron temperature behavior.

Figure 6 summarizes upflow velocity and flux at 75.2 °N geomagnetic latitude. They are sorted by small/large storms (in terms of Dst minimum) and CIR-driven/CME-driven storms. The numbers of samples were more than 600, except for small CME storm case and 1 day after the large CME storm onset (see Figure S3). In the cases of the small CIR storms, ion velocity and flux become high in the daytime (~110 m/s and ~1.0×10^{13} $m^{-2}s^{-1}$) on the first day of storm onsets (panels a1 and b1). The same characteristics are seen in the daytime under small CME storms (panels a3 and b3), although the number of samples is ~500 (see panel c1 of Figure S3). The upward ion velocity and flux gradually decrease under the small CIR storms, whereas the velocity and flux rapidly decrease one day after the small CME storms. On the first day of the

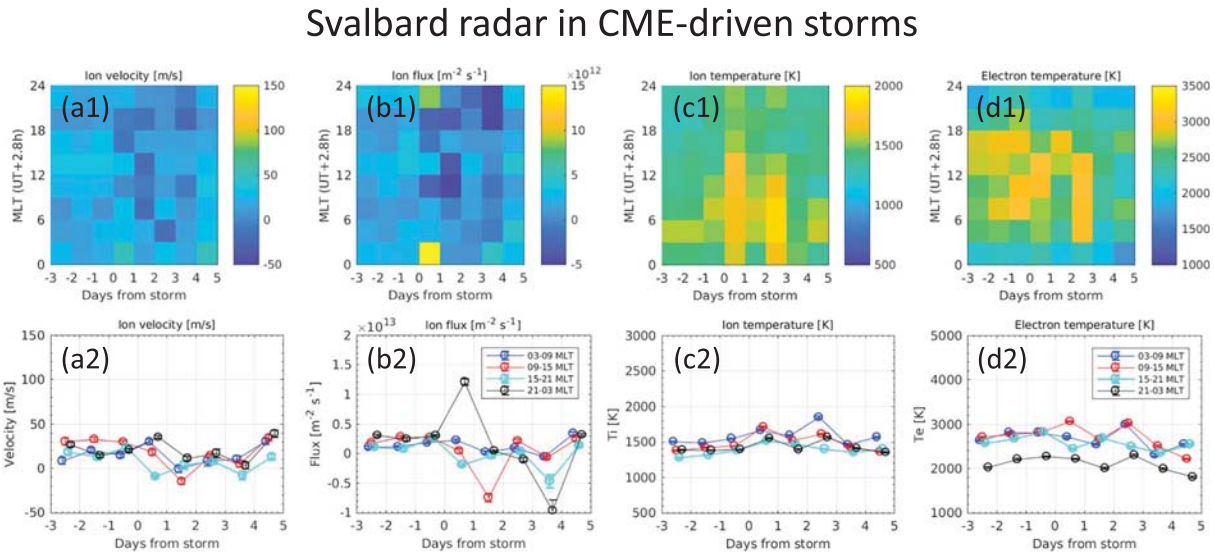

Figure 5. Same as Figure 4 except for CME-driven storms. CME = coronal mass ejection; MLT = magnetic local time; UT = Universal time.

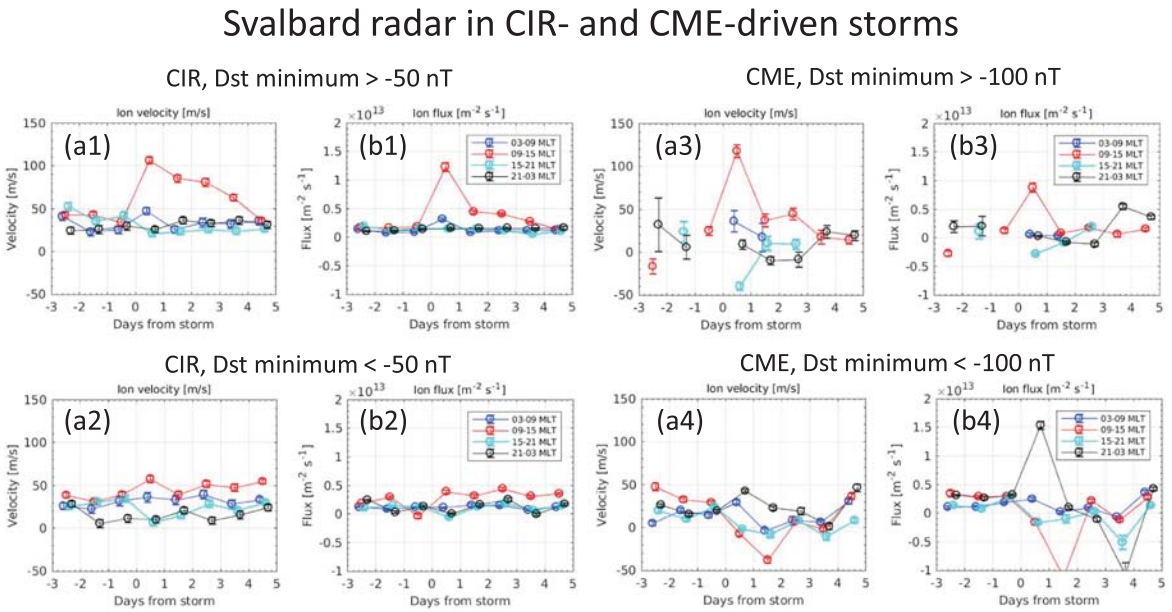

Figure 6. Averaged velocity and flux of upflowing ions measured with the EISCAT Svalbard radar. Formats of the plots are same as those of Figure 3. They are divided into four categories: (a1 and b1) CIR-driven small storms (Dst minimum > −50 nT), (a2 and b2) CIR-driven large storms (Dst minimum < −50 nT), (a3 and b3) CME-driven small storms (Dst minimum > −100 nT), and (a4 and b4) CME-driven large storms (Dst minimum < −100 nT). CIR = corotating interaction region; CME = coronal mass ejection; MLT = magnetic local time.

small CME storm onsets, downward ion flow is seen in the dusk region. The detailed comparison between the CIR-driven and CME-driven storms at this geomagnetic latitude is described in the Discussion section.

In the cases of the large storms, no clear upflow is seen in the daytime at this latitude. Ion velocity and flux in the daytime become slightly upward (~60 m/s and ~0.6×10^{13} $m^{-2}s^{-1}$) at the large CIR storm onsets (panels a2 and b2). They retain their values for a few days. During the large CME storms, ion downflows are typically seen in the daytime (panels a4 and b4). On the other hand, upward ion flux becomes extremely high (~$1.6 \times 10^{13} m^{-2}s^{-1}$) in the nighttime at the large CME storm onsets.

3.3. Summary of the EISCAT Observations at 66.2 °N and 75.2 °N Geomagnetic Latitudes

These results mentioned above are summarized in Table 1. At 66.2 °N geomagnetic latitude, upflowing ions are typically seen in the nighttime and dusk regions. Averaged ion fluxes are ~1.2×10^{13} $m^{-2}s^{-1}$ and

Table 1
Summary of Ion Upflow Flux at Each Region on the First Day of Magnetic Storm

66.2° mlat. (Tromsø)	CIR		CME	
	Small storm	Large storm	Small storm	Large storm
Dawnside	~0	~0	0.2	-
Daytime	~0	~0	0.2	~0
Duskside	0.2	0.2	0.2	0.5
Nighttime	0.3	0.2	1.2	3.3
75.2° mlat. (Longyearbyen, Svalbard)	**CIR**		**CME**	
	Small storm	Large storm	Small storm	Large storm
Dawnside	0.3	0.1	~0	0.2
Daytime	1.2	0.5	0.9	−0.2
Duskside	0.1	~0	−0.3	−0.2
Nighttime	0.1	~0	~0	1.5

Note. The unit of the ion flux is ($\times 10^{13}$ $m^{-2}s^{-1}$).

~3.3×10^{13} $m^{-2}s^{-1}$ under the small and large CME-driven storms, respectively, which are about 4–10 times higher than those under the CIR-driven storms, although averaged velocities under the CIR and CME storms are almost the same (50–80 m/s). This indicates that background ion density becomes high under the CME storms. At 75.2 °N geomagnetic latitude, an upward flux is always ~1.0×10^{13} $m^{-2}s^{-1}$ in the daytime, except for the case of the CME-driven large storms. Under the CME-driven large storm, nighttime upflow has a large flux (1.5×10^{13} $m^{-2}s^{-1}$). Downward ion fluxes are seen in the dayside and dusk regions under the CME-driven large storms.

4. Discussion

When large storms occur, the auroral oval expands equatorward so that EISCAT Svalbard radar (at 75.2° geomagnetic latitude) has a high chance to be located in the polar cap region. Thus, it is important to understand relative locations between the two radar positions, in terms of the convection pattern, and the large-scale field-aligned currents. These quantities also provide an important clue to understand the possible causes of the upflow. For these purposes, we utilized the Weimer model to estimate the FACs, the ionospheric electric fields, and the Joule heating rate at the radar sites.

Figure 7 summarizes the FACs, the ionospheric electric fields, and the Joule heating rate at 66.2 °N geomagnetic latitude (the same latitude of Tromsø UHF radar) together with IMF Bz, and the solar wind speed. Left panels show the results for the CIR-driven storms (panels a1–f1), which are comparable to the panel in Figure 1. Right ones show the results for the CME-driven storms (panels a2–f2), which are comparable to the panel in Figure 2. On the first day of the CIR-driven storms, the northward electric field is enhanced in the dusk region and the southward electric field is enhanced in the dawn region. The polarity of the electric field is consistent with the DP2 current system (two-cell convection), which probably results in the increase in the Joule heating rate (~8 mW/m^2). Small ion upflows and ion temperature enhancements observed by Tromsø UHF radar in the dawn (03–06 MLT) and dusk (15–18 MLT) regions (see Figures 1a–1c) are associated with those enhancements related to the two-cell convection during the CIR-driven storms. Before the CIR-driven storms, the downward (upward) FACs are seen on the duskside (dawnside), which probably corresponds to the Region 2 FAC defined by Iijima and Potemra (1976). The Region 1 sense FACs start to appear just after the CIR-driven storms, which probably corresponds to the equatorward expansion of the Region 1 FAC or newly developed Region 1 sense FACs.

In the case of the CME-driven storms, the Region 2 FAC is seen before the storms, while the Region 1 sense FAC is seen on the first day of the storms (Figure 7a2). This is probably understood as the equatorward expansion of the Region 1 FAC or newly developed Region 1 sense FACs. They also indicate that the EISCAT Tromsø UHF radar is situated under the Region 1 FAC, at least, in the dusk and dawn regions on the first day of storms. The Region 1 FAC persists for only 1–2 days over the EISCAT radar during the CME-driven storms, whereas the Region 1 FAC persists for several days during the CIR-driven storms. The panel d2 of Figure 7 shows that westward electric field is typically seen in the midnight region, corresponding to the region where upward flux is extremely high (see Figures 2b1 and 2b2). On the first day of CME-driven storms, the Joule heating rate drastically increases in the dusk region (15–18 MLT) and also increases in the nighttime region (Figure 7b2). Ion temperature also increased in the nighttime but not in the dusk region at Tromsø (see Figures 2c1 and 2c2). This indicates that it would be difficult to estimate the relative location of the EISCAT Tromsø UHF radar to the enhanced Joule heating region in the duskside from Weimer model on the first day of the CME-driven storm onset.

Note that the samples are not evenly distributed over the solar cycle and season for the CME-driven storms. The samples for the CME-driven storms were acquired in spring, autumn, and winter (not summer) near the solar maxima (1999–2003 and 2013–2015). Therefore, different solar cycle and seasonal conditions are mixed in the epoch analyses. In this particular study, we assume that the influence of the seasonal and solar cycle variations of the background conditions (such as ion/electron temperature) would be negligible. However, we admit that the background conditions may contribute to the result. When the large number of samples are successfully acquired in the future and the data is statistically significant, we will reanalyze them.

At 66.2 °N geomagnetic latitude, electron temperature increase is clearly seen in the nighttime on the first day of the CME-driven storm onset (see Figure 2d2). The increase seems to be larger than that under the

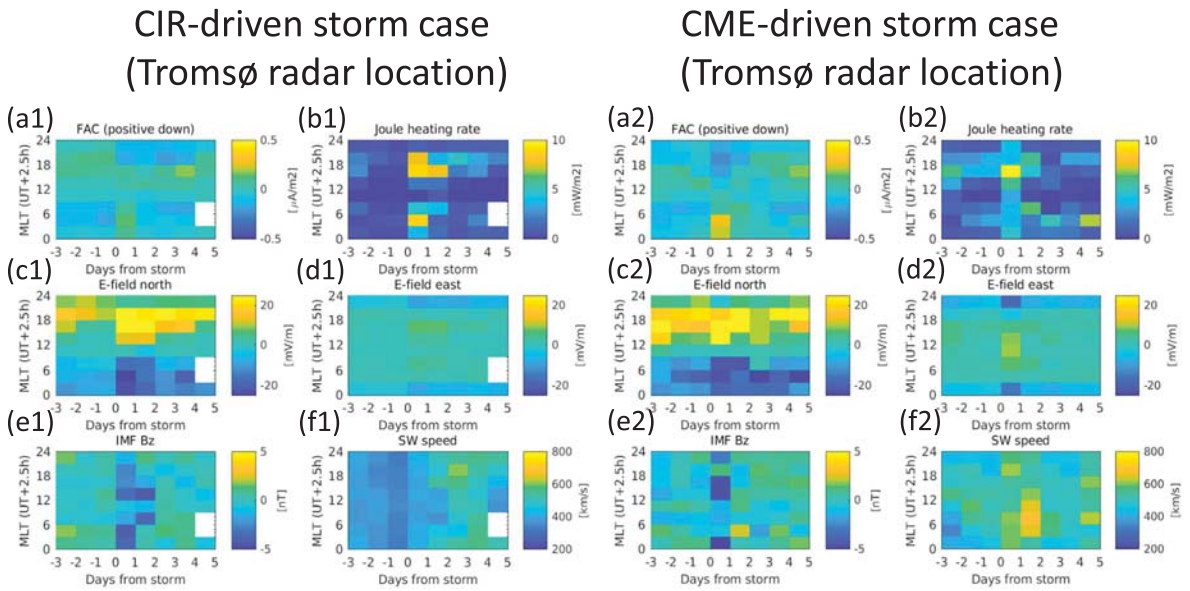

Figure 7. Averaged parameters derived from Weimer model at 66.2 °N geomagnetic latitude and solar wind parameters during CIR- and CME-driven storms. Left panels (a1–f1) are CIR case and right panels (a2–f2) are CME case. From top left to bottom right, (a) field-aligned current (positive downward), (b) Joule heating rate, (c) northward electric field, (d) eastward electric field, (e) IMF Bz, and (f) solar wind speed. Formats of the vertical and horizontal axes are same as panels a to d of Figures 1 and 2. CIR = corotating interaction region; CME = coronal mass ejection; FAC = field-aligned current; IMF = interplanetary magnetic field; MLT = magnetic local time; SW = solar wind; UT = Universal time.

CIR-driven storm. The increase is caused by soft (<500 eV) particle precipitation and heat flux from the magnetosphere (e.g., Caton et al., 1996), and it makes ions flow upward via enhanced ambipolar electric field in the topside ionosphere. The soft particle precipitation also causes electron and ion density enhancement in the *F* region and topside ionosphere and can make upward ion flux increase. This implies that the significant difference of upward fluxes under the CIR- and CME-driven storms is caused by different number fluxes of the soft particle precipitation.

Aikio et al. (2008) showed variations of electron and ion temperature in the vicinity of the polar cap boundary during late expansion and recovery of a substorm and their connection to ion outflow measured with Cluster spacecrafts in the magnetosphere (~3.4 R_E). The ion outflow coincides with a region of enhanced electron temperature rather than increased ion temperature in the *F* region ionosphere. The region of elevated ion temperature is limited in the vicinity of polar cap boundary. It also suggests that the strong upflows around midnight under CME-driven storms are mainly associated with enhancement of electron temperature caused by both soft particle precipitation and heat flux from the magnetosphere. The enhanced ion frictional heating due to strong electric fields may be additional contribution to the generation of ion upflow.

Figure 8 is the same as Figure 7 except at 75.2 °N geomagnetic latitude (the same latitude of the Svalbard radar). Again, the left panels are the results for CIR-driven storms (panels a1–f1), which are comparable to the panel in Figure 4. The right ones are the results for CME-driven storms (panels a2–f2), which are comparable to the panel in Figure 5. The Svalbard radar is most likely situated in the Region 1 FAC current region throughout the entire interval of interest. The Region 1 FACs increase in the daytime at the storm onsets during the CIR-driven storms, while they tend to decrease during the CME-driven storms. The latter indicates that the Svalbard radar moved to the poleward of the Region 1 FAC region during the CME-driven storms in association with an equatorward expansion of the auroral oval. Consequently, the Svalbard radar is situated in the polar cap (e.g., downward ion flows) as characterized by the enhancement of the eastward electric field (poleward convection on the dayside). During the CIR-driven storms, the direction of the electric field suddenly changes (panels c1 and d1) and the plasma flow direction becomes poleward in the dayside on the first day of storms, and consequently, the Joule heating rate slightly increases in the daytime (panel b1). The increased Joule heating rate lasts for a few days, as ion upflow continues for a few days. Note that distribution of the Joule heating rates on the first day of CIR-driven storm onset (panel b1)

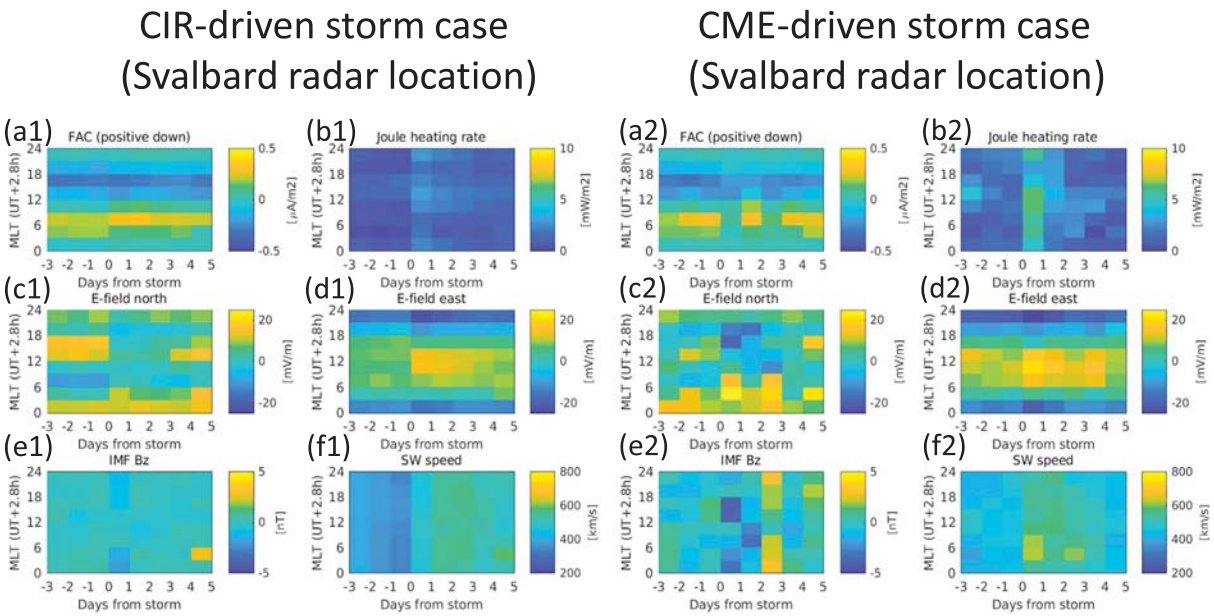

Figure 8. Same as Figure 7 except at 75.2 °N geomagnetic latitude. CIR = corotating interaction region; CME = coronal mass ejection; FAC = field-aligned current; IMF = interplanetary magnetic field; MLT = magnetic local time; SW = solar wind; UT = Universal time.

shows small enhancements in the daytime and nighttime, whereas ion temperature slightly increases in the daytime and morning (Figure 4c1). Typical plasma flow patterns at Longyearbyen have been statistically investigated with the Svalbard radar data by Cai et al. (2016), and the poleward flows and elevated Joule heating rate are seen in the dayside during southward IMF conditions (see Figure 3 of Cai et al., 2016).

During the CME-driven storms, nighttime upflows are typically seen on the first day of storms (see Figures 5b1 and 5b2). An increase of Joule heating rates on the first day of the CME-driven storm onset is larger than that of CIR-driven storm. Clear enhancements in the daytime for CME-driven storms are seen in Joule heating rates (Figure 8b2) and ion temperature (Figure 5c1). The upflows would be mainly caused by frictional heating in the *F* region ionosphere near the poleward edge of auroral oval. The case study by Ogawa et al. (2013) clearly shows such large upflows at the northward edge of aurora during the poleward expansion of auroral substorm. This study indicates that upward flux at this latitude becomes significant in nighttime during the first day of storms, although its velocity becomes small on average.

Because the Dst minimum values during the most of the CIR-driven storms are larger than −100 nT, the difference between the CIR-driven and CME-driven storms may come from the different Dst minima. To minimize the influence of the Dst minima, we compare the panels a2 and b2 of Figure 4 (for all CIR-driven storms) with the panels a3 and b3 of Figure 6 (for the CME-driven storms with a Dst minimum being larger than −100 nT). The most significant difference between them is found in the upflow velocities on the first day of the storms. The averaged ion velocity is about 120 m/s in the 09–15 MLT sector under the CME-driven storms, while that is about 80 m/s under the CIR-driven storms. Moreover, a downward velocity is found in the 15–21 MLT sector only in the CME-driven storms. These differences should be related to the combined effects: (1) temporal variations of ion upflow and (2) spatial variations of the Svalbard radar position relative to the auroral oval. The averaged IMF Bz was largely negative in the 15–21 MLT sector on the first day of CME-driven storms with a Dst minimum being larger than −100 nT (not shown here). The largely negative IMF Bz during the small CME-driven storms makes auroral oval expand, and the Svalbard radar observes downward ion flows at the dusk-sector in the polar cap region, just after the strong upflow in the daytime.

During large CME storms, downward ion flows are typically seen in the daytime at 75.2 °N geomagnetic latitude. Such downflow is frequently seen under largely negative IMF Bz and/or high solar wind pressure (e.g., Ogawa et al., 2009). It suggests the following scenario: During large CME storms (1) ion upflow region moves equatorward in the daytime, (2) ions in the upflow region convect poleward, and consequently, (3) the ions ballistically return downward at the Svalbard radar location.

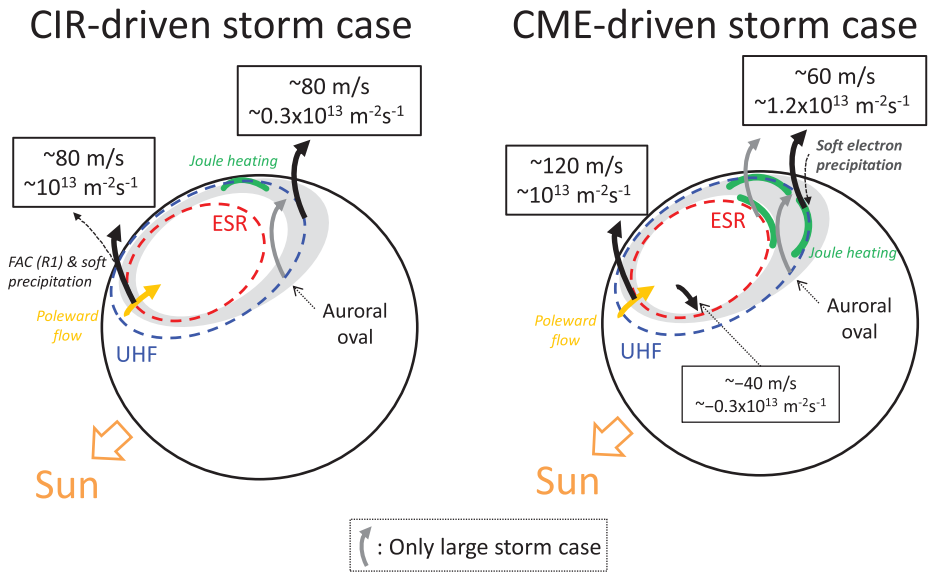

Figure 9. Schematic drawing of ion upflows in the polar ionosphere on the first day of CIR- and CME-driven storms. Averaged ion upflow/downflow velocity and flux during CIR- and CME-driven small storms are included. Gray arrows indicate typical upflow regions only during CIR- and CME-driven large storms. Note that ion upflow region moves equatorward in the daytime during CME-driven large storms. CIR = corotating interaction region; CME = coronal mass ejection.

Previous statistical studies of ion upflow at Tromsø show that occurrence frequency of upward ion velocity in excess of 100 m/s above 400-km altitude was about 10% around midnight (Foster et al., 1998; Keating et al., 1990). It suggests that average upward ion velocity should be smaller than 50 m/s even in the nighttime. This study shows that upward ion velocity clearly exceeds 50 m/s on average in the nighttime during the first day of both CIR- and CME-driven storm onsets, although the number of events was limited for this study (about 15 events in the nighttime for both CIR- and CME-driven storm cases). Another previous statistical study of ion upflow at Tromsø exhibits a dawn-dusk asymmetry above 400-km altitude, and it favors the dawn sector under disturbed condition (Liu et al., 2000). Our result also indicates that the average upflow velocity in the dawn region is slightly higher than that in the dusk region on the first day of CME-driven storm onset (Figure 2a2). A statistical study of Joule heating rate at Tromsø also shows that the Joule heating rate in the dawn region is higher than that in the dusk region under high geomagnetic activity period (Aikio & Selkälä, 2009). The characteristic is also reflected in our results: Ion temperature increases in the dawn region on the first day of the CIR-driven storm onset.

It is worth mentioning that upward ion flux is seen in the nighttime at 66.2 °N geomagnetic latitude before the CME-driven storm onsets (see Figures 2b1 and 2b2). As mentioned above, multiple storm events are excluded from our data set, so the nighttime upflows are probably related to the isolated substorms that could occur during nonstorm times. They can be fed into the plasma sheet and the inner magnetosphere before the storm onsets. The mass supply during pre-storm periods might affect the population of O^+ ions with local nonadiabatic acceleration in the inner magnetosphere during storms. We will investigate possible impacts of the prestorm ion upflows in future.

5. Conclusions

This paper showed variations of ionospheric ion upflow during CIR- and CME-driven storms, using a limited data set of the EISCAT Tromsø UHF and Svalbard radars during storm time between 1996 and 2015. Upward ion velocity and flux increase in the nighttime at 66.2 °N geomagnetic latitude just after the CIR- and CME-driven storms. CME-driven storms have larger upward ion flux (1.7×10^{13} $m^{-2}s^{-1}$) in the nighttime than that under CIR-driven storms (0.3×10^{13} $m^{-2}s^{-1}$). The significant difference of upward fluxes under the CIR- and CME-driven storms may be caused by different number fluxes of the soft particle

precipitation. Comparison results with the Weimer model indicate that Region 1-sense FACs start to appear at Tromsø latitude on the first day of both CIR- and CME-driven storm onsets.

At 75.2 °N geomagnetic latitude, upward ion velocity and flux are seen under small storm cases. Its upward velocity and flux are typically ~100 m/s and 10^{13} $m^{-2}s^{-1}$ for both CIR- and CME-driven small storms. Ion upflow under the CIR-driven small storms continues for a few days, whereas that under the CME-driven small storms has a large enhancement only on the first day of the storms. On the first day of the CME-driven large storm onset, ion upflows corresponding to ion temperature increase are typically seen in the nighttime and downward ion flows are seen in the daytime and duskside at this geomagnetic latitude. Results of the Weimer model at the same latitude show that the upflows under the CIR-driven storm associate with enhancements of the Region 1 FAC. Also, an enhancement of the eastward electric field (corresponding to poleward plasma flow on the dayside) is continuously seen in the daytime between the first and fourth days of the CIR- and CME-driven storm onsets.

The characteristics mentioned in these conclusions are summarized in Figure 9 for the CIR- and CME-driven storm cases. This basic knowledge about the response of the Earth's upper atmosphere to CME-driven and CIR-driven storms will contribute to understanding of the response of the upper atmosphere in other planets such as Mars and Venus.

Acknowledgments
This research was financially supported by the Grants-in-Aid for Scientific Research A (16H02229) and Young Scientists B (17K14400) by the Ministry of Education, Science, Sports, and Culture, Japan. The production of this paper was supported by an National Institute of Polar Research (NIPR) publication subsidy. This work was partially carried out at the joint research workshop of the Institute for Space-Earth Environmental Research, Nagoya University. EISCAT is an international association supported by research organizations in China (CRIRP), Finland (SA), Japan (NIPR), Norway (NFR), Sweden (VR), and the United Kingdom (NERC). All EISCAT radar data which we used in this study are available at the EISCAT database web page (http://pc115.seg20.nipr.ac.jp/www/eiscatdata/). Weimer model is developed by Daniel Weimer of Solana Scientific Inc. We used Dst and AL indexes from WDS Kyoto University at http://wdc.kugi.kyoto-u.ac.jp/, and the OMNI data obtained from the GSFC/SPDF OMNIWeb interface at https://omniweb.gsfc.nasa.gov/ website. Fruitful discussion with Y. Miyoshi about IMF Bz effects on the magnetosphere is also acknowledged.

References

Aikio, A. T., Pitkanen, T., Fontaine, D., Dandouras, I., Amm, O., Kozlovsky, A., et al. (2008). EISCAT and Cluster observations in the vicinity of the dynamical polar cap boundary. *Annales Geophysicae*, *26*, 87–105.

Aikio, A. T., & Selkälä, A. (2009). Statistical properties of Joule heating rate, electric field and conductances at high latitudes. *Annales Geophysicae*, *27*, 2661–2673.

Borovsky, J. E., & Denton, M. H. (2006). Differences between CME-driven storms and CIR-driven storms. *Journal of Geophysical Research*, *111*, A07S08. https://doi.org/10.1029/2005JA011447

Cai, L., Aikio, A. T., & Milan, S. E. (2016). Joule heating hot spot at high latitudes in the afternoon sector. *ournal of Geophysical Research: Space Physics*, *121*, 7135–7152. https://doi.org/10.1002/2016JA022432

Caton, R., Horwitz, J. L., Richards, P. G., & Liu, C. (1996). Modeling of F-region ionosphere upflows observed by EISCAT. *Geophysical Research Letters*, *23*, 1537.

Coley, W. R., & Heelis, R. A. (2009). Stormtime measurements of topside ionospheric upflow from Defense Meteorological Satellite Program. *Journal of Geophysical Research*, *114*, A10305. https://doi.org/10.1029/2009JA014350

Ebihara, Y., Yamada, M., Watanabe, S., & Ejiri, M. (2006). Fate of outflowing suprathermal oxygen ions that originate in the polar ionosphere. *Journal of Geophysical Research*, *111*, A04219. https://doi.org/10.1029/2005JA011403

Endo, M., Fujii, R., Ogawa, Y., Buchert, S. C., Nozawa, S., Watanabe, S., & Yoshida, N. (2000). Ion upflow and downflow at the topside ionosphere observed by the EISCAT VHF radar. *Annales Geophysicae*, *18*, 170.

Engwall, E., Eriksson, A. I., Cully, C. M., Andre, M., Puhl-Quinn, P. A., Vaith, H., & Torbert, R. (2009). Survey of cold ionospheric outflows in the magnetotail. *Annales Geophysicae*, *27*, 3185–3201.

Foster, C., Lester, M. T., & Davies, J. A. (1998). A statistical study of diurnal, seasonal and solar cycle variations of F-region and topside auroral upflows observed by EISCAT between 1984 and 1996. *Annales Geophysicae*, *16*, 1144–1158.

Gloeckler, G., Wilken, B., Studemann, W., Ipavich, F. M., Hovestadt, D., Hamilton, D. C., & Kremser, G. (1985). First composition measurement of the bulk of the storm-time ring current (1 to 300 keV/e) with AMPTE/CCE. *Geophysical Research Letters*, *12*, 325–328.

Grandin, M., Aikio, A. T., Kozlovsky, A., Ulich, T., & Raita, T. (2017). Cosmic radio noise absorption in the high-latitude ionosphere during solar wind high-speed streams. *Journal of Geophysical Research: Space Physics*, *122*, 5203–5223. https://doi.org/10.1002/2017JA023923

Hamilton, D. C., Gloeckler, G., Ipavich, F. M., Studemann, W., Wilken, B., & Kremser, G. (1988). Ring current development during the great geomagnetic storm of February 1986. *Journal of Geophysical Research*, *93*, 14,343–14,355.

Iijima, T., & Potemra, T. A. (1976). Large-scale characteristics of field-aligned currents associated with substorms. *Journal of Geophysical Research*, *81*, 3999.

Kataoka, R., & Miyoshi, Y. (2006). Flux enhancement of radiation belt electrons during geomagnetic storms driven by coronal mass ejections and corotating interaction regions. *Space Weather*, *4*, S09004. https://doi.org/10.1029/2005SW000211

Kavanagh, A. J., Honary, F., Donovan, E. F., Ulich, T., & Denton, M. H. (2012). Key features of >30 keV electron precipitation during high speed solar wind streams: A superposed epoch analysis. *Journal of Geophysical Research*, *117*, A00L09. https://doi.org/10.1029/2011JA017320

Keating, J., Mulligan, F. J., Doyle, D. B., Winser, K. J., & Lockwood, M. (1990). A statistical study of large field-aligned flows of thermal ions at high-latitudes. *Planetary and Space Science*, *38*(9), 1187–1201.

Keika, K., Kistler, L. M., & Brandt, P. C. (2013). Energization of O+ ions in the Earth's inner magnetosphere and the effects on ring current buildup: A review of previous observations and possible mechanisms. *Journal of Geophysical Research: Space Physics*, *118*, 4441–4464. https://doi.org/10.1002/jgra.50371

Liu, H., Schlegel, K., & Ma, S.-Y. (2000). Combined ESR and EISCAT observations of the dayside polar cap and auroral oval during the May 15, 1997 storm. *Annales Geophysicae*, *18*(9), 1067–1072.

Longden, N., Denton, M. H., & Honary, F. (2008). Particle precipitation during ICME-driven and CIR-driven geomagnetic storms. *Journal of Geophysical Research*, *113*, A06205. https://doi.org/10.1029/2007JA012752

Miyoshi, Y., Kataoka, R., Kasahara, Y., Kumamoto, A., Nagai, T., & Thomsen, M. F. (2013). High-speed solar wind with southward interplanetary magnetic field causes relativistic electron flux enhancement of the outer radiation belt via enhanced condition of whistler waves. *Geophysical Research Letters*, *40*, 1–6. https://doi.org/10.1002/grl.50916

Nilsson, H., Yamauchi, M., Eliasson, L., Norberg, O., & Clemmons, J. (1996). Ionospheric signature of the cusp as seen by incoherent scatter radar. *Journal of Geophysical Research*, *101*, 10947.

Nosé, M., Ohtani, S., Takahashi, K., Lui, A. T. Y., McEntire, R. W., Williams, D. J., et al. (2001). Ion composition of the near-Earth plasma sheet in storm and quiet intervals: Geotail/EPIC measurements. *Journal of Geophysical Research*, *106*, 8391–8403.

Nosé, M., Taguchi, S., Hosokawa, K., Christon, S. P., McEntire, R. W., Moore, T. E., & Collier, M. R. (2005). Overwhelming O+ contribution to the plasma sheet energy density during the October 2003 superstorm: Geotail/EPIC and IMAGE/LENA observations. *Journal of Geophysical Research*, *110*, A09S24. https://doi.org/10.1029/2004JA010930

Ogawa, Y., Buchert, S. C., Fujii, R., Nozawa, S., & van Eyken, A. P. (2009). Characteristics of ion upflow and downflow observed with the European Incoherent Scatter Svalbard radar. *Journal of Geophysical Research*, *114*, A05305. https://doi.org/10.1029/2008JA013817

Ogawa, Y., Buchert, S. C., Sakurai, A., Nozawa, S., & Fujii, R. (2010). Solar activity dependence of ion upflow in the polar ionosphere observed with the European Incoherent Scatter (EISCAT) Tromsø UHF radar. *Journal of Geophysical Research*, *115*, A07310. https://doi.org/10.1029/2009JA014766

Ogawa, Y., Fujii, R., Buchert, S. C., Nozawa, S., & Ohtani, S. (2003). Simultaneous EISCAT Svalbard radar and DMSP observations of ion upflow in the dayside polar ionosphere. *Journal of Geophysical Research*, *108*, 1101. https://doi.org/10.1029/2002JA009590

Ogawa, Y., Sawatsubashi, M., Buchert, S. C., Hosokawa, K., Taguchi, S., Nozawa, S., et al. (2013). Relationship between auroral substorm and ion upflow in the nightside polar ionosphere. *Journal of Geophysical Research: Space Physics*, *118*, 7426. https://doi.org/10.1002/2013JA018965

Rietveld, M. T., Wright, J. W., Zabotin, N., & Pitteway, M. L. V. (2008). The Tromso dynasonde. *Polar Science*, *2*(1), 55–71.

Seki, K., Elphic, R. C., Hirahara, M., Terasawa, T., & Mukai, T. (2001). On atmospheric loss of oxygen ions from earth through magnetospheric processes. *Science*, (5510), 1939–1941.

Weimer, D. R. (2005). Improved ionospheric electrodynamic models and application to calculating Joule heating rates. *Journal Of Geophysical Research*, *110*, A05306. https://doi.org/10.1029/2004JA010884

Wilson, G. R., Ober, D. M., Germany, G. A., & Lund, E. J. (2004). Nightside auroral zone and polar cap ion outflow as a function of substorm size and phase. *Journal of Geophysical Research*, *109*, A02206. https://doi.org/10.1029/2003JA009835

Erratum

During production, unit of flux was changed in error from "$m^{-2}s^{-1}$" to "m^2/s." Unit of flux indicates "per square meter per second" and the original "m^{-2} s^{-1}" was correct. This error has been corrected throughout the article, and this may be considered the official version of record.